






Silicate Grain Growth due to Ion Trapping in Oxygen-rich Supernova Remnants like Cassiopeia A

Florian Kirchschlager , M. J. Barlow , and Franziska D. Schmidt 

Department of Physics and Astronomy, University College London, Gower Street, London WC1E 6BT, UK; f.kirchschlager@ucl.ac.uk
Received 2019 November 15; revised 2020 March 5; accepted 2020 March 6; published 2020 April 16

Abstract

Core-collapse supernovae can condense large masses of dust post-explosion. However, sputtering and grain–grain collisions during the subsequent passage of the dust through the reverse shock can potentially destroy a significant fraction of the newly formed dust before it can reach the interstellar medium. Here we show that in oxygen-rich supernova remnants like Cassiopeia A, the penetration and trapping within silicate grains of the same impinging ions of oxygen, silicon, and magnesium that are responsible for grain surface sputtering can significantly reduce the net loss of grain material. We model conditions representative of dusty clumps (density contrast of $\chi = 100$) passing through the reverse shock in the oxygen-rich Cassiopeia A remnant and find that, compared to cases where the effect is neglected as well as facilitating the formation of grains larger than those that had originally condensed, ion trapping increases the surviving masses of silicate dust by factors of up to two to four, depending on initial grain radii. For higher density contrasts ($\chi \gtrsim 180$), we find that the effect of gas accretion on the surface of dust grains surpasses ion trapping, and the survival rate increases to $\sim 55\%$ of the initial dust mass for $\chi = 256$.

Unified Astronomy Thesaurus concepts: [Astrophysical dust processes \(99\)](#); [Interstellar dust processes \(838\)](#); [Core-collapse supernovae \(304\)](#); [Supernova remnants \(1667\)](#); [Hydrodynamics \(1963\)](#)

1. Introduction

The formation of dust in core-collapse supernova ejecta has been established for at least three decades (Lucy et al. 1989). Along with SN 1987A and the Crab Nebula, Cassiopeia A (Cas A) is the most studied dusty supernova remnant (SNR). The remnant of an explosion from around the year 1680, at a distance of ~ 3.4 kpc, has a diameter of ~ 3.4 pc today (Reed et al. 1995). Within Cas A, dense gas clumps and knots are observed that are associated with the location of freshly produced dust (Lagage et al. 1996; Rho et al. 2012). Strong emission features in the mid-infrared (IR) spectra of Cas A have been identified with siliceous grains by Rho et al. (2008), consistent with the very oxygen-rich composition of its ejecta (Chevalier & Kirshner 1979).

The total dust mass in the ejecta has been derived by different observational strategies to be between $\sim 0.1M_{\odot}$ and $\sim 1M_{\odot}$ (Dunne et al. 2009; Barlow et al. 2010; Sibthorpe et al. 2010; Bevan et al. 2017; De Looze et al. 2017; Priestley et al. 2019), while a theoretical study of dust formation and evolution predicted Cas A’s dust mass to be of the order of $0.08M_{\odot}$ (Nozawa et al. 2010). This apparent discrepancy between theory and observations is accompanied by a difference in estimated grain sizes: supernova dust grain radii derived from IR emission fitting, as well as from fits to asymmetric optical line profiles, are of the order of $0.1 \mu\text{m}$ up to a few microns (Stritzinger et al. 2012; Fox et al. 2015; Owen & Barlow 2015; Wesson et al. 2015; Bevan & Barlow 2016; Priestley et al. 2020), while dust formation theories predict grain sizes to be $\lesssim 0.1 \mu\text{m}$ (Todini & Ferrara 2001; Nozawa et al. 2003; Bianchi & Schneider 2007; Marassi et al. 2015; Biscaro & Cherchneff 2016).

Aggravating this situation, the interaction of the blast wave with the circumstellar and interstellar medium causes a reverse shock (Gotthelf et al. 2001), which can have a crucial effect on the evolution of the embedded dust material. Significant amounts of dust can be destroyed or transformed when

the reverse shock encounters the dusty ejecta clumps (e.g., Nozawa et al. 2010; Silvia et al. 2010; Bocchio et al. 2016; Micelotta et al. 2016). Recently, Kirchschlager et al. (2019, hereafter K19) have studied dust survival rates in Cas A as a function of clump densities, dust material, and initial grain size distributions. They found that grain–grain collisions and sputtering are synergistic and that grain–grain collisions have a strong influence on the dust survival rate by fragmenting larger grains to smaller particles that are more easily destroyed by sputtering.

Ion implementation and trapping in dust grains has not been considered so far as a process that, in suitable environments, can counteract grain destruction by sputtering. The gas in the ejecta clumps of Cas A is composed of $\sim 80\%$ oxygen with contributions from Ne, Mg, Si, S, and Ar and a negligible amount of hydrogen and helium (Willingale et al. 2002; Docenko & Sunyaev 2010). Chevalier & Kirshner (1979) detected dense knots that are made of almost pure oxygen. Due to the high gas temperatures and shock velocities, energetic oxygen and other heavy ions can penetrate deep into the grains. For grain temperatures below ~ 500 K, the diffusion rate of oxygen atoms in silicates is very low (Brady 2013) and thus they will be trapped once they have intruded into the grain. This will automatically lead to grain growth and an increase in dust mass. Therefore, grain growth by ion trapping can potentially counteract destructive processes, such as thermal and kinematic sputtering as well as fragmentation and vaporization in grain–grain collisions.

In this paper, the effect of ion trapping on the dust evolution in Cas A is studied. In Section 2, we describe our model setup and give a summary of the considered dust processes. We introduce oxygen ion trapping in dust grains in Section 2.4. The results of our study are presented in Section 3 and a summarizing conclusion is given in Section 4.

2. Model and Methods

2.2. Dust Model

In order to investigate the effect of oxygen ion trapping in dust grains in the ejecta of Cas A, we performed hydrodynamical simulations using the grid-based code ASTROBEAR (Carroll-Nellenback et al. 2013). ASTROBEAR simulations model only the gas phase (Section 2.1) and we use our external post-processing code PAPERBOATS (K19) to investigate dust motions as well as dust grain growth or dust destruction in a high-velocity, hot gas environment (Sections 2.2–2.4).

2.1. Cloud-crushing Problem

The applied model is based on the setup used in K19 and is briefly summarized here.

Instead of simulating the entire SN ejecta, we consider only a section of it. We focus on the cloud-crushing scenario (Woodward 1976; Silvia et al. 2010) in which a planar shock is driven into an overdense spherical clump of gas that is embedded in a low-density ambient medium (see Figure 2 in K19). The interaction between this reverse shock and the clump is assumed to be of a similar nature for all ejecta clumps ($\sim 10^5$ – 10^6 in total; see K19) so that our results can be applied and projected to them. Following this approach, we are able to investigate the destruction of a single clump at higher spatial resolution. The initial (pre-shock) conditions comprise the clump radius of $R_{\text{cl}} = 10^{16}$ cm; uniform gas number densities in the ambient medium of $n_{\text{am}} = 1 \text{ cm}^{-3}$, while in the clump $n_{\text{cl}} = \chi n_{\text{am}}$, where χ is the density ratio between clump gas and ambient medium gas; along with the gas temperatures in the ambient medium and in the clump, $T_{\text{am}} = 10^4$ K and $T_{\text{cl}} = 10^2$ K, respectively. Unless stated otherwise, we set $\chi = 100$. The shock velocity in the ambient medium is adopted to be $v_{\text{sh}} = 1600 \text{ km s}^{-1}$ (Micelotta et al. 2016), which transforms to be $\sim 160 \text{ km s}^{-1}$ in the clump, and the mean molecular weight of the pre-shock gas is $\mu_{\text{gas}} = 16$, which corresponds to pure oxygen gas.

The simulation is executed for three cloud-crushing times, $\tau_{\text{cc}} = \chi^{0.5} R_{\text{cl}} / v_{\text{sh}}$ (Klein et al. 1994), after the first contact of the shock with the clump, which gives the characteristic time for the clump to be crushed and evolved by the shock. For the chosen initial conditions, the simulation time is then ~ 61.5 yr. In contrast to K19, we perform not only 2D but also 3D simulations. The computational domain consists of 420×140 and $420 \times 140 \times 140$ cells, respectively, representing a box of length $l_{\text{box}} = 21 R_{\text{cl}} = 0.068$ pc and width $w_{\text{box}} = 7 R_{\text{cl}} = 0.023$ pc, and for the 3D simulations with a box height $h_{\text{box}} = w_{\text{box}}$. The post-shock gas conditions are then calculated by ASTROBEAR using the Rankine–Hugoniot jump conditions taking into account radiative cooling for a gas of pure oxygen (see Figure 3 in K19). The shock evolves in the direction of l_{box} and the given box size ensures that the clump material stays in the domain throughout the entire simulation.

At this resolution, the 2D and 3D simulations of the cloud-crushing problem show only moderate differences, which is why we present here only the 3D results. We expect more subtle variations between 2D and 3D at higher resolution but we are limited to 20 cells per clump radius due to the large computational effort for highly resolved 3D post-processing simulations (Section 2.3).

The grains in our study are spherical with grain radius a . At the start, the grain sizes follow a log-normal distribution (e.g., Nozawa et al. 2003) that is described by the radius a_{peak} at which the distribution has its maximum and the dimensionless quantity σ that defines the width of the distribution. We fix $\sigma = 0.1$ and vary a_{peak} to 0.01, 0.1, and $1 \mu\text{m}$. The grain size distribution spans from $a_{\text{min,abs}} = 0.6 \text{ nm}$ to $a_{\text{max,abs}} = 10 \mu\text{m}$ and is discretized in 40 log-spaced size bins. The dust material is silicate and the material parameters required for the dust post-processing are given in Table 2 of K19. Initially, the dust is at rest compared to the clump gas and homogeneously distributed in the clump with a gas-to-dust mass ratio of $\Delta_{\text{gd}} = 10$ (Priestley et al. 2019) while the ambient medium is dust-free.

2.3. Dust Processing

We use our parallelized 3D external dust processing code PAPERBOATS (K19) to determine the dust evolution in the shocked clump based on the time and spatially resolved gas density, velocity, and temperature output of ASTROBEAR as well as on the initial dust conditions (Section 2.2). We give here a short overview of the processes considered and refer to K19 for a detailed description.

PAPERBOATS was developed to simulate dust motions in the shocked clump as well as dust destruction and grain growth processes. The dust is accelerated by the streaming gas taking into account both collisional and plasma drag (Baines et al. 1965; Draine & Salpeter 1979). Destruction processes include fragmentation and vaporization in grain–grain collisions (e.g., Tielens et al. 1994; Jones et al. 1996) as well as thermal and nonthermal (kinematic) sputtering (e.g., Barlow 1978; Bocchio et al. 2014). As the dust temperatures in Cas A are of the order of or even below 100 K (De Looze et al. 2017; Priestley et al. 2019), dust destruction by evaporation can be neglected.

Besides the dust destruction processes, two grain growth processes were also previously considered: the coagulation of dust grains and the accretion of (dusty) gas onto the surfaces of the grains. Both can occur, either at low relative velocities in a grain–grain collision or when the energy E of an impinging gas particle is below the threshold energy E_{sp} for the sputtering of grain atoms (Bohdansky et al. 1980; Tielens et al. 1994). For the latter case, the gas particle can be accreted in a process akin to negative sputtering. Sticking in grain–grain collisions has a negligible effect on the dust processing, as the present grain velocities are mostly too high (K19).

On the other hand, when the ion impact energy is sufficiently high, gas particles penetrate into the dust grains and can be trapped. This potential grain growth scenario has not been considered so far for the dust evolution in oxygen-rich SNRs and will be outlined in the following section.

2.4. Oxygen Ion Trapping

We have added oxygen ion trapping in dust grains as an additional feature to the sputtering routine of PAPERBOATS. The sputtering models commonly used in the astronomical literature (e.g., Tielens et al. 1994; Nozawa et al. 2006) only describe the number of detached dust atoms per incident gas particle but do not consider the further progress of the incident gas particle.

Due to the energetic ion bombardment that silicate grains experience in the reverse shock, they should be rendered partially disordered, enabling impacting and subsequently trapped gas atoms of O, Si, Mg, etc. to form new silicate structure bonds with the surrounding grain material atoms. Along with $10\ \mu\text{m}$ silicate emission features, the oxygen-rich SNRs Cas A and G54.1-0.3 both exhibit an unusual $21\ \mu\text{m}$ dust emission feature that has been attributed to a number of siliceous grain materials, including SiO_2 and MgSiO_3 (Rho et al. 2008, 2018) and $\text{Mg}_{0.7}\text{SiO}_{2.7}$ (Temim et al. 2017). The constituent atoms of each of those materials have a mean atomic weight of $\mu_{\text{dust}} = 20$ (in atomic mass units m_{amu}). From its X-ray spectrum, Willingale et al. (2002) derived gas-phase abundance number ratios for Cas A of $\text{Si}/\text{O} = 0.34$ and $\text{Mg}/\text{O} = 0.063$, corresponding to a mean atomic weight of 19.3. Heavier species, such as Ca and Fe, will raise the mean atomic weight of impacting ions further. So for such oxygen-rich SNRs, we can treat the mean atomic weight of implanted atoms and sputtered atoms as being the same. For convenience, hereafter the trapping of ions of various elements will be referred to as oxygen trapping, which is the most abundant element.

2.4.1. Penetration Depth

When the energy of the gas particle is high enough, it can penetrate into the dust grain. The penetration depth r_p of the gas particle into the dust grain can be calculated using the Bethe–Bloch formalism (see Section 4.6.6 in K19) and depends, beside the particle energy, on the dust material parameters and the ionization degree of gas and dust grain. Oxygen is the predominant gas species in Cas A’s ejecta and has a diffusion timescale (per nanometer) that is much longer than the Hubble time in olivine or quartz grains with dust temperatures of the order of $\sim 500\ \text{K}$ or less (Brady 2013).

We set the minimum penetration depth that is required to enable oxygen trapping to $r_{\text{min}} = 5$ layers of silicate particles ($\sim 1.1\ \text{nm}$). This number is an assumption; however, we have tested lower limits of $r_{\text{min}} = 0, 3, 10$ and 20 silicate layers and found that the differences in the net yield are negligible for $r_{\text{min}} \leq 5$ layers while $r_{\text{min}} = 10$ and 20 layers show significantly reduced oxygen trapping. We note that a minimum penetration depth of five silicate layers corresponds to an energy of $\sim 30\ \text{eV}$ (which is similar to the sputtering threshold energy E_{sp}) for a fully ionized oxygen ion. An impinging oxygen ion with $160\ \text{km s}^{-1}$ corresponds to $2.1\ \text{keV}$ and a penetration depth of $\sim 70\ \text{nm}$ (see Figure 10 in K19 for the relation between the penetration depth and ion energy).

On the other hand, the penetration depth of the oxygen particle has to be below the extent of the grain. The geometrically averaged path length through the grain is given by $r_{\text{max}} = 4/3$ grain radii, which we use as an upper limit.

2.4.2. Net Yield

The yield, Y , is the change of the number of dust grain atoms per normal incident gas particle. A positive yield represents dust destruction by sputtering while a negative yield implies dust grain growth by gas accretion (low energy) or ion trapping (high energy).

When the conditions for oxygen ion trapping are fulfilled ($r_{\text{min}} \leq r_p \leq r_{\text{max}}$), the oxygen ions cause a negative yield of $Y_{\text{trap}} = -1$. The net yield resulting from sputtering (Y_{sp}) and

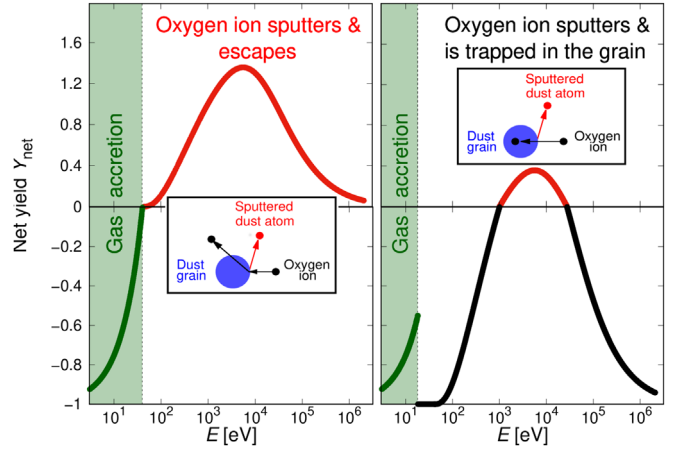


Figure 1. Net yield, Y_{net} , that gives the change of number of atoms in the grain per incident oxygen ion as a function of energy E of the incident oxygen ion. A positive yield corresponds to dust destruction; a negative yield corresponds to dust growth. When the energy of the incident oxygen ion is higher than the sputtering threshold energy, E_{sp} , dust atoms can be sputtered. Left: trapping conditions are not fulfilled (oxygen particle escaping after the sputtering event) so the resulting net yield is equal to the regular sputtering yield, $Y_{\text{net}} = 2Y_{\text{sp}}$ (red solid line). Right: the oxygen ion is trapped so the net yield amounts to $Y_{\text{net}} = 2Y_{\text{sp}} - 1$ (black solid line), which can become negative as less than 1 silicate atom is detached per sputtering event. For both cases, the incident oxygen atom is accreted at lower energies (green shaded region).

trapping (Y_{trap}) amounts to $Y_{\text{net}} = 2Y_{\text{sp}} - 1$ where a factor of two is considered to allow for higher measured sputtering yields at non-normal incidence over normal incidence sputtering yields (e.g., Tielens et al. 1994). Y_{sp} is usually below 1 for oxygen particles impacting on various dust materials (silicate, carbon, etc.; see Tielens et al. 1994), so the net yield can become negative (right panel of Figure 1). If the oxygen particle is not trapped by the grain the net yield amounts to the regular sputtering yield, $Y_{\text{net}} = 2Y_{\text{sp}}$ (left panel of Figure 1).

For energies lower than the sputtering energy threshold, E_{sp} , and lower than the energy at which trapping can occur, gas particles are assumed to be accreted onto the grain surface with a yield of $Y_{\text{acc}} = -(1 - E/E_{\text{sp}})$ (K19). The linear decay of the gas accretion yield enables a continuous transition from the gas accretion to the sputtering regime at the threshold energy, E_{sp} (left panel of Figure 1). When the energy of the impinging oxygen particle is below E_{sp} but still high enough that it can be trapped, the net yield is set to $Y_{\text{net}} = -1$.

Finally, the resulting net yield amounts to

$$Y_{\text{net}} = \begin{cases} 2Y_{\text{sp}}, & \text{if } (E > E_{\text{sp}}) \wedge \text{not trapped,} \\ 2Y_{\text{sp}} - 1, & \text{if } (E > E_{\text{sp}}) \wedge \text{trapped,} \\ -1, & \text{if } (E < E_{\text{sp}}) \wedge \text{trapped,} \\ Y_{\text{acc}}, & \text{if } (E < E_{\text{sp}}) \wedge \text{not trapped.} \end{cases} \quad (1)$$

2.4.3. Gas Depletion Factor

Sputtering, gas accretion, and gas trapping cause a change of the grain size a to $a - \left(\frac{da}{dt}\right)\Delta t$ during the time-step, Δt , where

$$\frac{da}{dt} = \frac{\mu_{\text{dust}} m_{\text{amu}}}{4\rho_{\text{bulk}}} (D_{\text{gas}} n_{\text{gas}}) \langle Y_{\text{net}} v \rangle_{\text{skM}}, \quad (2)$$

(Barlow 1978; Draine & Salpeter 1979; Tielens et al. 1994; Nozawa et al. 2006; Bocchio et al. 2014) is the reduction of grain radius per unit time, $\mu_{\text{dust}} = 20$ is the mean atomic weight

of silicate grain atoms, m_{amu} is the atomic mass unit, ρ_{bulk} is the dust bulk density, n_{gas} is the gas number density, and $\langle Y_{\text{net}} v \rangle_{\text{skM}}$ is the product of the net yield and velocity, v , averaged over the skewed Maxwellian velocity distribution. We introduce here a gas depletion factor:

$$D_{\text{gas}} = \frac{\tau_d}{\Delta t} \left(1 - \exp \left[-\frac{\Delta t}{\tau_d} \right] \right), D_{\text{gas}} \in [0, 1] \quad (3)$$

with

$$\tau_d = (\pi a^2 n_a \langle -(Y_{\text{acc}} + Y_{\text{trap}}) v \rangle_{\text{skM}})^{-1} \quad (4)$$

as the gas depletion timescale and n_a as the number density of dust grains with radius a . Considering a typical number density $n_a = 0.01 \text{ m}^{-3}$ for grains with radius $a = 0.1 \mu\text{m}$ (for a clump gas density of $n_{\text{cl}} = 100 \text{ cm}^{-3}$, a gas-to-dust mass ratio of $\Delta_{\text{gd}} = 10$, and an initial log-normal distribution with $a_{\text{peak}} = 0.1 \mu\text{m}$ and $\sigma = 0.1$), $\langle Y_{\text{acc}} + Y_{\text{trap}} \rangle \approx -1$, and a velocity of the dust relative to the gas of the order of $v = 10 \text{ km s}^{-1}$, the gas depletion timescale amounts to $\tau_d \approx 10^4 \text{ yr}$. However, as small dust grains are generated due to dust fragmentation, the number density of 1 nm grains in shocked and compressed clumps can take values up to the order of $n_a \sim 10^6 \text{ m}^{-3}$, and the resulting depletion timescale is then only $\tau_d \approx 1 \text{ yr}$, which is comparable to the used time-step of $\Delta t = 0.5 \text{ yr}$. The high post-shock gas temperatures cause even higher velocities v and thus reduce the gas depletion timescale which becomes crucial for the further evolution.

For regular sputtering, the gas particles are not trapped or accreted ($Y_{\text{acc}} = Y_{\text{trap}} = 0$) and the gas number density n_{gas} is unaffected so that the depletion factor is 1. However, when gas accretion or trapping are present, oxygen atoms are removed from the gas and the gas number density decreases during the time-step, Δt . To take that into account, the actual gas number density in Equation (2) is $D_{\text{gas}} n_{\text{gas}}$ (see the Appendix for a derivation of D_{gas}).

Due to the nature of the post-processing, we are not able to reduce the gas number density from one time-step to the next as this would strongly affect the hydrodynamical simulations. Therefore, we are limited to considering gas depletion only for the calculation of the yields and we have to neglect the evolution of gas depletion on a longer timescale. Moreover, we also neglect the destroyed dust material that contributes to the regular gas and was introduced by K19 as “dusty gas.” Test simulations have shown that the production of new grain material by ion trapping together with destruction of the material by sputtering or grain–grain collisions could lead, under extreme conditions, to an unrealistically high dusty gas density that would, at least at the end of our simulations, completely dominate the evolution of both the gas and dust component. The main reason for this high dusty gas density is the fact that we cannot follow the depletion of the regular gas. Therefore, the gas would serve as an inexhaustible source of material resulting in unrealistically high gas trapping and accretion rates. On the other hand, we expect that the disregard of the dusty gas component counters the continuous refreshing of the regular gas component and that both effects cancel each other out: when dust destruction by sputtering and dust growth by ion trapping and accretion are at similar levels, the sum of the gas mass and the dust grain mass is fixed.

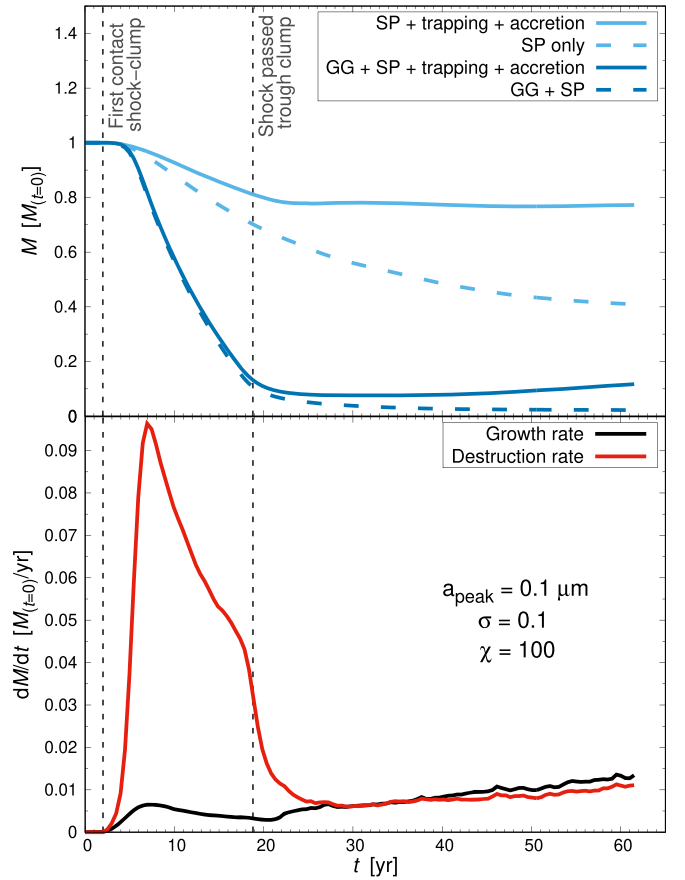


Figure 2. Top: surviving dust mass, M , of the clump in units of the initial clump dust mass, $M_{(t=0)}$, as a function of time, taking into account grain–grain collisions (GG) and sputtering (SP) with or without trapping or accretion of oxygen ions (different colors and line types). Oxygen trapping and gas accretion reduce the dust destruction significantly. Bottom: dust destruction and growth rates as a function of time. Both sputtering and grain–grain collisions are considered for the dust destruction while the dust growth is given by the mass of trapped or accreted oxygen per unit time. The difference between these two rates determines the total dust mass evolution in the top panel (solid dark-blue line). The time points when the shock has first contact with the clump as well as when it has traveled through the clump are indicated in both panels as vertical dashed lines.

3. Results

We conducted 3D hydrodynamical simulations of the cloud-crushing problem using ASTROBEAR and determined the integrated dust mass as a function of time using PAPERBOATS.

The impact of ion trapping and gas accretion on the total dust survival rate can be clearly seen in Figure 2 (top panel). When the shock impacts the clump, the combined effects of grain–grain collisions and sputtering rapidly decrease the total dust mass. The destruction weakens after ~ 1 cloud-crushing time ($\sim 20 \text{ yr}$) and the remaining dust mass is mostly maintained. Taking ion trapping and gas accretion into account, the total dust mass even starts to increase slightly after the first cloud-crushing time and reaches $\sim 12\%$ of the original mass after three cloud-crushing times. For comparison, when ion trapping and accretion are neglected, the dust survival rate decreases during the entire simulation time and ends up at only $\sim 3\%$. Neglecting grain–grain collisions, $\sim 80\%$ of the initial dust mass survives for the case of sputtering combined with ion trapping while the survival rate is $\sim 40\%$ for sputtering without ion trapping and accretion. Ion trapping and gas accretion increase the surviving dust mass fraction.

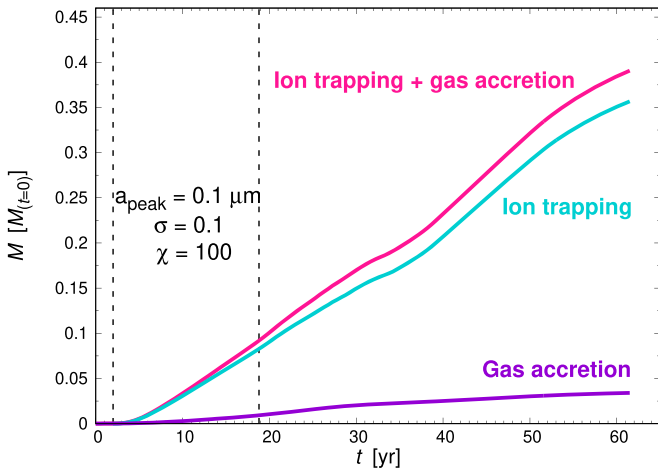


Figure 3. Dust mass, M (in units of the initial clump dust mass, $M_{(t=0)}$), gained by ion trapping and/or accretion of the gas as a function of time. The plots do not take into account that a significant part of the newly produced dust masses could be destroyed again by sputtering or grain–grain collisions.

Figure 2 (bottom panel) shows the dust growth rate, $\dot{M}_{\text{growth}}(t)$, due to oxygen ion trapping and accretion as well as the rate of destruction, $\dot{M}_{\text{destr}}(t)$, through sputtering and grain–grain collisions. The difference between them determines the total dust mass via $M(t + \Delta t) = M(t) + (\dot{M}_{\text{growth}}(t) - \dot{M}_{\text{destr}}(t))\Delta t$. In the first cloud-crushing time, the shock travels through the clump causing high temperatures and velocities, which result in a high destruction rate. Afterward, the clump decays and small-scale structures (of the order of ~ 1 mpc) with high gas densities are formed. The dust material is concentrated in these gas clumps, forming high dust density structures: dust growth as well as destruction processes are roughly at the same level in this environment. Dust growth slightly surpasses dust destruction at later times, which is one of the few differences between the 3D and 2D simulations: for the latter, the dust destruction and growth rates flatten after ~ 50 yr (not shown).

Oxygen trapping is the dominant growth process compared to gas accretion (Figure 3). The mass gained by ion trapping increases linearly with time and reaches $\sim 35\%$ of the initial clump dust mass, $M_{(t=0)}$, after three cloud-crushing times. In comparison, the newly produced dust mass due to gas accretion amounts to $0.03 M_{(t=0)}$ at the end of the simulation. At around two cloud-crushing times, ion trapping is reinforced due to the reduced relative velocities between gas and dust components, and the mass gained by ion trapping rises slightly stronger. In total, ion trapping makes up $\sim 90\%$ of the newly produced dust mass after three cloud-crushing times. The accreted gas material will be predominantly located close to the surface of the grains where it can be more easily destroyed by, e.g., sputtering than by trapped atoms inside the grains. Thus the contribution of the ion trapping to the dust mass gain is even higher.

Figure 4 shows the spatial distribution of the gas and of $0.1 \mu\text{m}$ silicate grains with or without oxygen trapping and accretion for one, two, and three cloud-crushing times after the shock has impacted the clump. The maps represent the central cut of the 3D domain through the initial center of the clump. In the case of ion trapping and accretion, the dust component has higher densities but also higher density contrasts (overdense knots) compared to the case of no ion trapping or accretion. The equivalent maps in 2D (not shown) have gas and dust

density distributions that are less evolved in the shock direction but broader perpendicular to the shock direction. We emphasize not only that the maps in Figure 4 only depict the distribution of $0.1 \mu\text{m}$ radius grains but that due to the dust processing, grains of much smaller or larger radii (at least for the case of oxygen trapping) can be formed. Consequently, the maps for other grain sizes are significantly different and indicate regions of enhanced rates of dust production or destruction.

A comparison between simulations for different initial log-normal grain size distributions with $a_{\text{peak}} = 0.01, 0.1,$ and $1 \mu\text{m}$ (Figure 5) shows that the surviving dust mass depends strongly on the initial size distribution of the grains (22%, 12%, and 5%, respectively). This is because the effect of oxygen ion trapping and accretion is a function of grain size that can be explained by the dependence of the depletion timescale, τ_d , on the grain radius for a fixed dust-to-gas mass ratio. The effect of the grain size on the quantity $\langle -(Y_{\text{acc}} + Y_{\text{trap}})v \rangle_{\text{skM}}$ is negligible and the timescale for gas depletion is then proportional to $(a^2 n_a)^{-1}$ (Equation (4)). As the initial dust mass is fixed, it follows $n_a \propto a^{-3}$ and $\tau_d \propto a$. The larger the initial grain sizes, the smaller the effects of ion trapping and gas accretion are and thus the surviving dust mass.¹

The dust mass of all three distributions is primarily destroyed within the first cloud-crushing time before ion trapping and accretion mitigate the destruction and even starts to increase the dust mass. Two effects are visible in Figure 5: oxygen ion trapping and accretion are more efficient for smaller grain sizes, as well as the fact that the evolution of larger grains is delayed compared to small grains. Grain destruction in the simulations for $a_{\text{peak}} = 1 \mu\text{m}$ grains starts ~ 5 yr after the destruction begins for initial distributions with $a_{\text{peak}} = 0.01$ and $0.1 \mu\text{m}$, as grain–grain collisions are the main destruction mechanism for these large grains and their stopping time, and thus their time to be accelerated, is of the order of years.

The dust processing completely redistributes the grain size distribution after three cloud-crushing times (Figure 6, left panel). On the one hand, destruction processes produce smaller grains compared to the initial grain size distribution; on the other hand, dust growth processes result in an increase of larger dust grains. K19 found that the final grain size distribution is composed of two components—a remnant of the initial distribution, located around a_{peak} but reduced in grain number density due to sputtering and collisions, plus a power-law distribution of smaller dust grains that reflect the fragments of shattering collisions. Through ion trapping and gas accretion, the power-law distribution is extended to larger grains than a_{peak} , at least for the simulations with $a_{\text{peak}} = 0.01$ and $0.1 \mu\text{m}$ for which oxygen trapping and accretion are efficient. As a comparison in Figure 6 (right panel), we show the final grain size distribution for simulations without oxygen trapping or gas accretion, clearly indicating a reduced number of large grains (surviving rates of 12%, 3%, and 3% for $a_{\text{peak}} = 0.01, 0.1,$ and $1 \mu\text{m}$, respectively).

For a density ratio of $\chi = 100$, the velocity of the reverse shock within the clump amounts to $\sim 160 \text{ km s}^{-1}$. The kinetic energy of a 160 km s^{-1} oxygen ion is of the order of 2.1 keV ,

¹ We note that this is a consequence of the fixed initial dust mass in the clump, which results in a larger dust cross section (integrated over all particles) the smaller the dust grain size. Furthermore, the initial dust grains must have a minimum grain radius in order to survive the impact of the shock during the first cloud-crushing time.

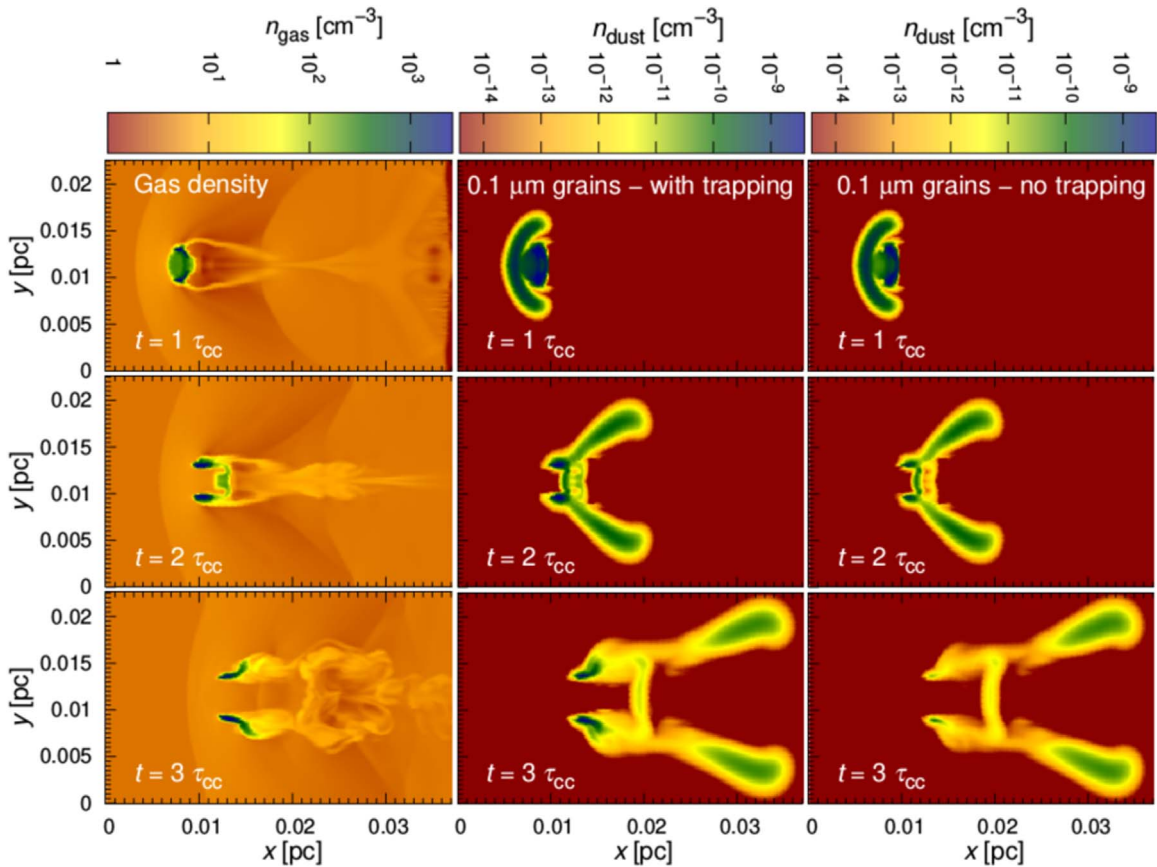


Figure 4. Temporal evolution of the spatial gas density (left column) as well as the number density of $0.1 \mu\text{m}$ dust grains, with (center) and without oxygen trapping (right). The rows show the distributions at time $t = 1, 2,$ and 3 cloud-crushing times, τ_{cc} , respectively, after the first contact of the reverse shock with the clump. The panels show a fixed cutout of the computational domain and the color scale is fixed for each figure column.

which corresponds to a net destruction of grain material (Figure 1). In contrast, a density ratio² of $\chi = 256$ causes a decrease of the shock velocity to 100 km s^{-1} within the clump, and oxygen ions of that velocity have a kinetic energy of 0.84 keV , which corresponds to a net gain of grain material. Consequently, we expect a more effective ion trapping mechanism as well as a larger surviving dust mass for the higher density contrast.

We conducted hydrodynamical simulations followed by dust post-processing for the density contrast $\chi = 256$ (Figures 7–9). As expected, the dust survival rates are larger than for $\chi = 100$. For $a_{\text{peak}} = 0.1 \mu\text{m}$, $\sim 55\%$ of the initial dust mass survives when ion trapping and gas accretion are taken into account ($\sim 12\%$ for $\chi = 100$), while the survival rate is below 1% without these mechanisms ($\sim 3\%$ for $\chi = 100$).

Grain–grain collisions destroy only a minor part of the dust material (K19) but cause the production of smaller fragments. As the survival rate drops below 10% in the first $\sim 35 \text{ yr}$, the grains must be destroyed by sputtering. In the case of ion trapping, the net yield at 0.84 keV is negative (see Figure 1), which implies dust growth for each impinging oxygen ion.

² An oxygen ion with velocity 100 km s^{-1} has a kinetic energy of 0.84 keV , at which the net yield is negative in the case of ion trapping (Figure 1, right). The grain effectively grows for each ion that impacts with that or lower velocity. The shock in the ambient medium has a velocity of $v_{\text{sh}} = 1600 \text{ km s}^{-1}$ and is decelerated in the clump to $v_{\text{sh,cl}} = v_{\text{sh}}/\sqrt{\chi}$. The oxygen ions can thus reach velocities up to 100 km s^{-1} when the density contrast amounts to $\chi = (v_{\text{sh}}/v_{\text{sh,cl}})^2 = (1600/100)^2 = 256$.

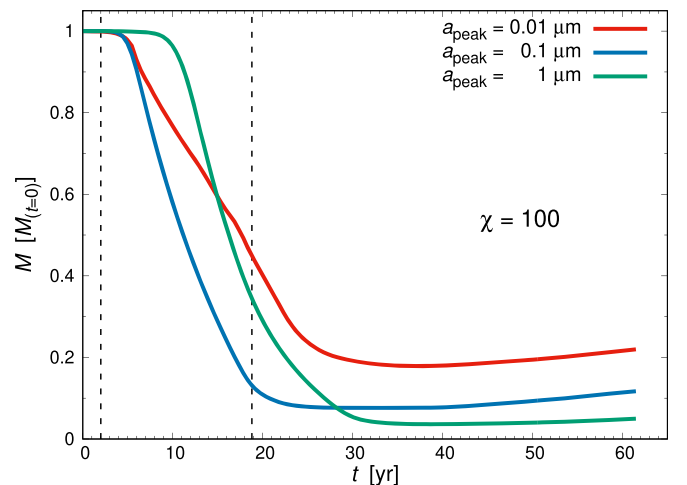


Figure 5. Surviving dust mass, M , in a clump in units of the initial clump dust mass, $M_{(t=0)}$, as a function of time for different initial log-normal grain size distributions, given by peak radii $a_{\text{peak}} = 0.01 \mu\text{m}$ (red solid line), $0.1 \mu\text{m}$ (blue), and $1 \mu\text{m}$ (green), and width of the initial distribution is $\sigma = 0.1$. Grain–grain collisions and sputtering with oxygen ion trapping and gas accretion are considered.

However, not all ions can be trapped as some instead tunnel through the small dust grains created by grain–grain collisions.

Figure 8 shows that the total mass gained is about $\sim 90\%$ of the initial clump dust mass ($\chi = 256$), which is twice the gained mass of the density contrast of $\chi = 100$. However, gas accretion makes a larger contribution (74%) than ion trapping

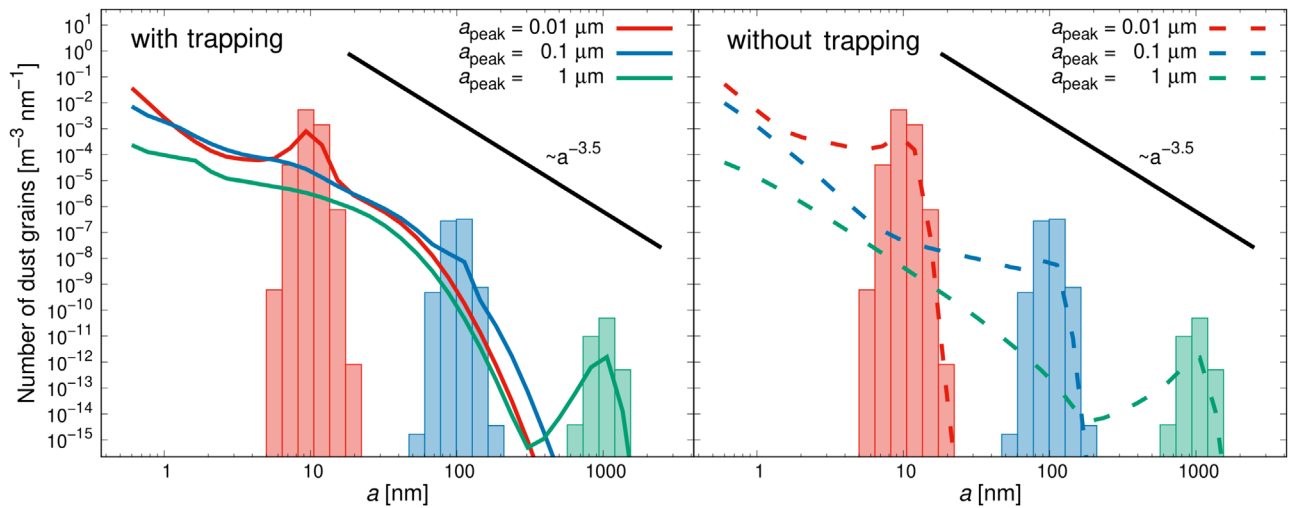


Figure 6. Final grain size distributions for initial log-normal distributions with $a_{\text{peak}} = 0.01, 0.1,$ and $1.0 \mu\text{m}$ (red, blue, and green lines, respectively; density contrast is $\chi = 100$) and a distribution width of $\sigma = 0.1$, with (left panel) and without (right panel) ion trapping or accretion. The initial distributions are shown as histograms and the slope of the common $\gamma = -3.5$ power-law is also shown.

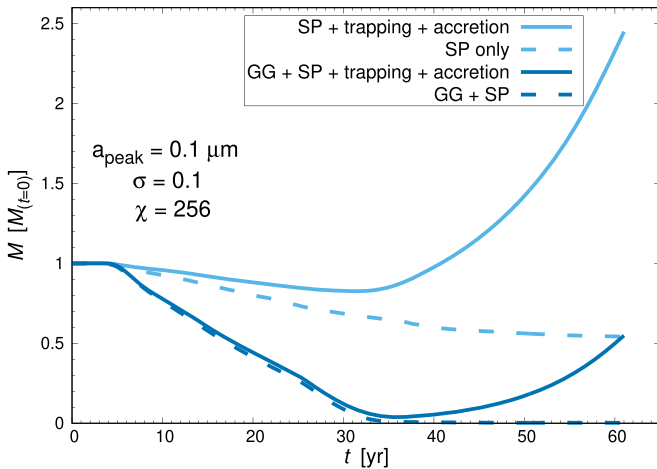


Figure 7. Same as Figure 2 (top panel) but for $\chi = 256$.

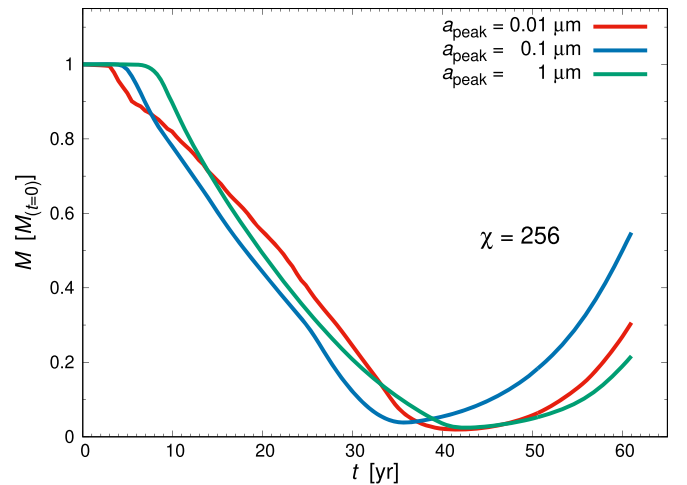


Figure 9. Same as Figure 5 but for $\chi = 256$.

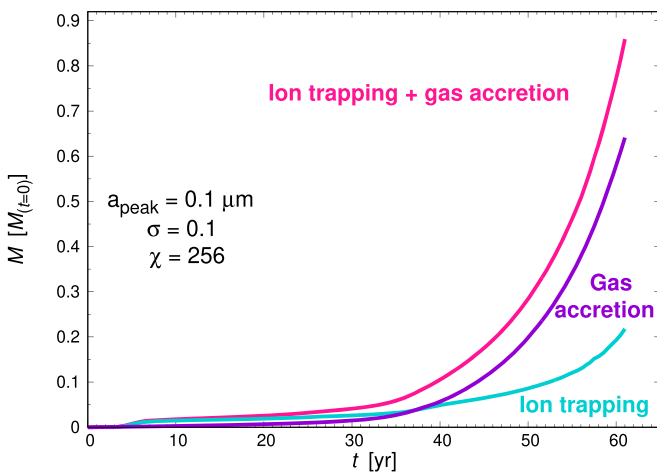


Figure 8. Same as Figure 3 but for $\chi = 256$. The plots do not take into account that a significant part of the newly produced dust masses could be destroyed again by sputtering or grain–grain collisions.

(26%). The reason is that $\sim 100 \text{ km s}^{-1}$ is the maximum velocity of the oxygen ions, which predominantly occurs at the moment when the reverse shock impacts the clump and hits the

unaccelerated dust grains. At later time points, the average velocities are lower and the energies of the oxygen ion are not sufficient for ion trapping but instead favor gas accretion. Therefore, the efficiency of ion trapping is also strongly dependent on the clump density and the shock velocity. Furthermore, the different gas density has an effect on the grain size dependence of the dust growth processes. Figure 9 shows that initial grain distributions with $a_{\text{peak}} = 0.1 \mu\text{m}$ have the highest survival rates for the density contrast of $\chi = 256$.

Gas accretion makes a larger contribution to the gained mass than ion trapping when the density contrast is $\chi = 256$, while the situation is the opposite for $\chi = 100$. Consequently, a critical density contrast at which gas accretion becomes more important than ion trapping exists. We conducted hydrodynamical simulations followed by dust post-processing (an initial log-normal grain size distribution with $a_{\text{peak}} = 0.1 \mu\text{m}$ and $\sigma = 0.1$) for the density contrasts $\chi = 140, 180,$ and 220 and determined the dust mass gained by ion trapping and gas accretion (Figure 10). With increasing density contrast, the dust mass gained due to oxygen trapping is in a rough decreasing trend while the accreted mass increases. At the density contrast $\chi \approx 180$, the mass gains from both effects are at a similar level

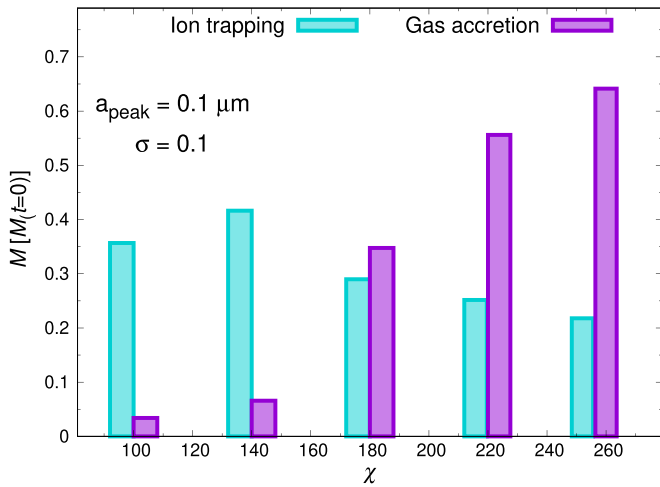


Figure 10. Gained dust mass due to oxygen trapping and gas accretion as a function of density contrast χ .

($\sim 0.3 M_{(t=0)}$). As gas accretion and ion trapping are both functions of the grain size, the critical density contrast depends on the initial grain size distribution.

4. Conclusions

We have investigated the influence of trapping of oxygen and other ions on the survival rate of dust grains through the passage of the reverse shock in the ejecta of the SNR Cas A. We found that oxygen trapping has the potential to significantly increase the surviving dust mass. In the case of a clump to ambient medium gas density contrast of $\chi = 100$ and an initial log-normal grain size distribution with a peak radius of $a_{\text{peak}} = 0.01 \mu\text{m}$ (0.1 and $1 \mu\text{m}$), the silicate survival rate is 12% (3% and 3%) when oxygen trapping and gas accretion are neglected but is 22% (12% and 5%) when these effects are taken into account. For larger density contrasts ($\chi \gtrsim 180$ for $a_{\text{peak}} = 0.1 \mu\text{m}$), the efficiency of gas accretion can surpass that of ion trapping in generating new dust material, resulting in higher survival rates.

The dust grain growth processes can produce a significant amount of grains that have sizes above the initial grain sizes. Therefore, ion trapping and gas accretion can play a crucial role in the surviving dust budget of oxygen-rich SNRs and thereby contribute to the dust budget in the interstellar medium. Finally, the increased grain sizes might account for the discrepancy between observed and theoretically predicted dust grain sizes in some SNRs.

F.K., M.J.B., and F.S. acknowledge funding from the European Research Council Grant SNDUST ERC-2015-AdG-694520. We would like to thank Erica Fogerty for providing generous support in the application of AstroBEAR. Simulations were performed using the UCL HPC RC cluster GRACE and the data intensive PETA4-SKYLAKES service at Cambridge. PETA4-SKYLAKES usage is supported through DiRAC project ACSP190 (SNDUST) using the Cambridge Service for Data Driven Discovery (CSD3), part of which is operated by the University of Cambridge Research Computing on behalf of the STFC DiRAC HPC Facility (www.dirac.ac.uk). The DiRAC component of CSD3 was funded by BEIS capital funding via STFC capital grants ST/P002307/1 and ST/R002452/1 and STFC operations grant ST/R00689X/1. DiRAC is part of the

National e-Infrastructure. We thank Clare Jenner (UCL), Lydia Heck (Durham University), UCL RC support, and Cambridge HPCS support for their assistance.

Software: Paperboats (Kirchschlager et al. 2019), AstroBEAR (Carroll-Nellenback et al. 2013), UCL HPC RC cluster GRACE, Peta4-Skylake (DiRAC project; www.dirac.ac.uk).

Appendix Derivation of the Gas Depletion Factor

We present here the derivation for the gas depletion factor D_{gas} (Equation (3)). Due to ion trapping and gas accretion, the gas number density $\tilde{n}_{\text{gas}}(t)$ decreases during each time-step Δt as an e-folding function of time, $\tilde{n}_{\text{gas}}(t) = \exp\left[-\frac{t}{\tau_d}\right]n_{\text{gas}}$, with $n_{\text{gas}} = \tilde{n}_{\text{gas}}(0)$ as initial gas density at each time-step and τ_d as the gas depletion timescale (Equation (4)). To take into account the changing gas density during Δt for the sputtering and trapping processes, we introduce the gas depletion factor D_{gas} which is the average gas density during the time interval $[0, \Delta t]$ divided by n_{gas} . Following the mean value theorem, $D_{\text{gas}}n_{\text{gas}}$ is the integral of $\tilde{n}_{\text{gas}}(t)$ with bounds 0 and Δt divided by the length of the interval,

$$D_{\text{gas}} = \frac{1}{\Delta t} \int_0^{\Delta t} \exp\left[-\frac{t'}{\tau_d}\right] dt' = \left(1 - \exp\left[-\frac{\Delta t}{\tau_d}\right]\right) \frac{\tau_d}{\Delta t}.$$

We note that the gas depletion factor D_{gas} can also be derived in a second approach taking into account mass conservation between the reduced gas mass on the one hand and the increase of dust mass that is generated due to gas accretion and trapping on the other hand.

ORCID iDs

Florian Kirchschlager <https://orcid.org/0000-0002-3036-0184>
M. J. Barlow <https://orcid.org/0000-0002-3875-1171>
Franziska D. Schmidt <https://orcid.org/0000-0003-2521-8834>

References

- Baines, M. J., Williams, I. P., & Asebiomo, A. S. 1965, *MNRAS*, 130, 63
Barlow, M. J. 1978, *MNRAS*, 183, 367
Barlow, M. J., Krause, O., Swinyard, B. M., et al. 2010, *A&A*, 518, L138
Bevan, A., & Barlow, M. J. 2016, *MNRAS*, 456, 1269
Bevan, A., Barlow, M. J., & Milisavljevic, D. 2017, *MNRAS*, 465, 4044
Bianchi, S., & Schneider, R. 2007, *MNRAS*, 378, 973
Biscaro, C., & Cherchneff, I. 2016, *A&A*, 589, A132
Bocchio, M., Jones, A. P., & Slavin, J. D. 2014, *A&A*, 570, A32
Bocchio, M., Marassi, S., Schneider, R., et al. 2016, *A&A*, 587, A157
Bohdansky, J., Roth, J., & Bay, H. L. 1980, *JAP*, 51, 2861
Brady, J. B. 2013, *Diffusion Data for Silicate Minerals, Glasses, and Liquids* (Washington, DC: American Geophysical Union), 269
Carroll-Nellenback, J. J., Shroyer, B., Frank, A., & Ding, C. 2013, *JCoPh*, 236, 461
Chevalier, R. A., & Kirshner, R. P. 1979, *ApJ*, 233, 154
De Looze, I., Barlow, M. J., Swinyard, B. M., et al. 2017, *MNRAS*, 465, 3309
Docenko, D., & Sunyaev, R. A. 2010, *A&A*, 509, A59
Draine, B. T., & Salpeter, E. E. 1979, *ApJ*, 231, 77
Dunne, L., Maddox, S. J., Ivison, R. J., et al. 2009, *MNRAS*, 394, 1307
Fox, O. D., Smith, N., Ammons, S. M., et al. 2015, *MNRAS*, 454, 4366
Gothelf, E. V., Koralesky, B., Rudnick, L., et al. 2001, *ApJL*, 552, L39
Jones, A. P., Tielens, A. G. G. M., & Hollenbach, D. J. 1996, *ApJ*, 469, 740
Kirchschlager, F., Schmidt, F. D., Barlow, M. J., et al. 2019, *MNRAS*, 489, 4465
Klein, R. I., McKee, C. F., & Colella, P. 1994, *ApJ*, 420, 213

- Lagage, P. O., Claret, A., Ballet, J., et al. 1996, *A&A*, **315**, L273
- Lucy, L. B., Danziger, I. J., Gouiffes, C., & Bouchet, P. 1989, in IAU Coll. 120, *Structure and Dynamics of the Interstellar Medium*, ed. G. Tenorio-Tagle, M. Moles, & J. Melnick (Berlin: Springer), 164
- Marassi, S., Schneider, R., Limongi, M., et al. 2015, *MNRAS*, **454**, 4250
- Micelotta, E. R., Dwek, E., & Slavin, J. D. 2016, *A&A*, **590**, A65
- Nozawa, T., Kozasa, T., & Habe, A. 2006, *ApJ*, **648**, 435
- Nozawa, T., Kozasa, T., Tominaga, N., et al. 2010, *ApJ*, **713**, 356
- Nozawa, T., Kozasa, T., Umeda, H., Maeda, K., & Nomoto, K. 2003, *ApJ*, **598**, 785
- Owen, P. J., & Barlow, M. J. 2015, *ApJ*, **801**, 141
- Priestley, F. D., Barlow, M. J., & De Looze, I. 2019, *MNRAS*, **485**, 440
- Priestley, F. D., Barlow, M. J., De Looze, I., & Chawner, H. 2020, *MNRAS*, **491**, 6020
- Reed, J. E., Hester, J. J., Fabian, A. C., & Winkler, P. F. 1995, *ApJ*, **440**, 706
- Rho, J., Gomez, H. L., Boogert, A., et al. 2018, *MNRAS*, **479**, 5101
- Rho, J., Kozasa, T., Reach, W. T., et al. 2008, *ApJ*, **673**, 271
- Rho, J., Onaka, T., Cami, J., & Reach, W. T. 2012, *ApJL*, **747**, L6
- Sibthorpe, B., Ade, P. A. R., Bock, J. J., et al. 2010, *ApJ*, **719**, 1553
- Silvia, D. W., Smith, B. D., & Shull, J. M. 2010, *ApJ*, **715**, 1575
- Stritzinger, M., Taddia, F., Fransson, C., et al. 2012, *ApJ*, **756**, 173
- Temim, T., Dwek, E., Arendt, R. G., et al. 2017, *ApJ*, **836**, 129
- Tielens, A. G. G. M., McKee, C. F., Seab, C. G., & Hollenbach, D. J. 1994, *ApJ*, **431**, 321
- Todini, P., & Ferrara, A. 2001, *MNRAS*, **325**, 726
- Wesson, R., Barlow, M. J., Matsuura, M., & Ercolano, B. 2015, *MNRAS*, **446**, 2089
- Willingale, R., Bleeker, J. A. M., van der Heyden, K. J., Kaastra, J. S., & Vink, J. 2002, *A&A*, **381**, 1039
- Woodward, P. R. 1976, *ApJ*, **207**, 484